doi:10.20944/preprints202002.0226.v1

Article

Triplet test on rubble stone masonry: numerical assessment of the shear mechanical parameters

Michele Angiolilli [1] **and Amedeo Gregori** [1,*]

[1] Department of Civil, Building and Environmental Engineering, University of L'Aquila, L'Aquila, Italy; michele.angiolilli@graduate.univaq.it

* Correspondence: amedeo.gregori@univaq.it, +390862434141

Abstract: Rubble stone masonry walls are widely diffused in most of the cultural and architectural heritage of historical cities. The mechanical response of such material is rather complicated to predict due to their composite nature. Vertical compression tests, diagonal compression tests, and shear-compression tests are usually adopted to experimentally investigate the mechanical properties of stone masonries. However, further tests are needed for the safety assessment of these ancient structures. Since the relation between normal and shear stresses plays a major role in the shear behavior of masonry joints, governing the failure mode, triplet test configuration was here investigated. First, the experimental tests carried out at the laboratory (LPMS) of the University of L'Aquila on stone masonry specimens were presented. Then, the triplet test was simulated by using the Total Strain Crack Model, which reflects all the ultimate states of quasi-brittle material such as cracking, crushing and shear failure. The goal of the numerical investigation was to evaluate the shear mechanical parameters of the masonry sample, including strength, dilatancy, normal and shear deformations. Furthermore, the effect of (i) confinement pressure and (ii) bond behavior at the sample-plates interfaces were investigated, showing that they can strongly influence the mechanical response of the walls.

Keywords: unreinforced masonry; quasi-brittle material; in-plane behavior; shear-compression; triplet test; dilatancy; bond behavior; confinement; finite element model; macro-model

---

1. Introduction

In the past, the traditional architecture of Mediterranean countries extensively used the stone, especially limestone, giving rise to one of the most important parts of the historical heritage, despite the serious damage inflicted by recurring earthquakes [1–5].

The extreme vulnerability of stone masonry buildings is mainly due to the mortar joints which represent the weak zone in masonry systems [6]. The weakness of the mortar joints is particularly relevant in the case of strong units combined with weak mortar joints that is the typical condition in the case of ancient stone masonries [7].

Although in the last decades several laboratory and in situ tests were performed on stone masonry walls, the mechanical behavior of stone masonries is still not completely characterized due to a lack of experimental data [8]. Indeed, due to the composite nature of the ancient masonry structures, the high irregularity of elements and the complex distributions of mortar joints, the mechanical response of irregular stone walls are difficult to be reproduced both in experimental tests and in numerical simulations. Here, it is worth highlighting the great effort made in some recent studies [9,10] to correlate the quality of the masonry walls to their mechanical properties. It is common practice employ vertical compression [11–14], diagonal compression [8,11,15–17] and shear-compression [18,19] tests to experimentally investigate the mechanical properties of stone masonries. However, further tests are needed to obtain useful data for safety assessment studies of ancient masonry structures [8].

Several experimental studies have been carried out on the bond shear strength of unit–mortar interfaces [20,21] and natural rock joints [7,22,23], but limited research is available on the shear behavior of stone masonry joints. The knowledge gathered can be partly extended to the present study knowing that the surface roughness plays an important role in the shear behavior of stone masonries.

One can find few experimental campaigns carried out by using the triplet test for rubble stone masonries (see [8,24]), in which reliable experimental evaluation of shear parameters is difficult to perform since results may be scattered because the mortar joints are not regularly arranged. However, the triplet test may be considered as a valid alternative to the other destructive tests due to the smaller size of the specimen required. The smaller specimen size, the easier operation and the smaller costs (and the invasiveness in case of existing building) are. Indeed, the size of the specimen tested under the triplet test can be assumed equal to about 50 mm in length and 50 mm in height (see [8,24]) and is more than two times smaller than the other tests. Thus, the triplet test may overcome the limitations of the other destructive tests that not allow an extensive characterization.

The goal of the study carried out in the present work was to investigate the most important mechanical parameters governing the shear behavior of the traditional rubble stone masonry walls. In particular, first, the paper presents results from triplet tests carried out at the laboratory LDPM of the University of L'Aquila (Italy). Then, numerical simulations are presented to better understand the mechanical behavior of stone masonry under the triplet test, also investigating the effect of the confinement pressure and the bond behavior at the masonry-plates interface. The conclusions of the present study offer the possibility to improve the experimental mechanical characterization of stone masonry structures and the modeling of them.

2. Description of the triplet test

The triplet test allows the evaluation of the shear strength parameters of the bed joints of the masonry. That test can be effective to generate shear failure, through the mortar of the masonry specimen, especially in case of strong units combined to weak mortar joints, which represent the most frequent condition in ancient stone masonries. Indeed, for this masonry type, the mechanism failure mainly regards the mortar joints, which represent the weak zone in masonry systems [6,7]. Triplet test relies on a particular constraint system that creates a shear box [24]. Usually, a couple of "L-shape" rigid steel plates are mounted on the upper and lower parts of the wall specimen (see Figure 1a). Then, a combined application of vertical pressure on the upper plate and a horizontal force on the unconstrained lateral edge of the specimen causes the slide of the central zone of the sample on two horizontal surfaces (see Figure 1b).

An important issue related to the experimental characterization of joint shear behavior concerns

The testing setup is an important issue to comprehend the experimental characterization of the shear behavior of mortar joint of masonry walls [25]. Indeed, as highlighted in [26], results are sensitive to the support conditions used. Although distinct loading arrangements have been used, it is difficult to provide uniform shear and normal stresses distribution along the joint so that failure occurs simultaneously at all points of the mortar joint [27]. That condition can be obtained by reducing the eccentricity of the reactions that may develop as close as possible to the unit-mortar interfaces [25]. The standard shear test method, also called the triplet test (EN1052-3 [28]), provides the best testing setup for the evaluation of the shear parameters of masonry walls. However, differently from brick masonries, such test is difficult to perform for stone masonry because the rocking phenomenon caused by the irregularity of the stone arrangement may preclude the shear sliding.

An important aspect regarding shear tests is the dilatancy ψ, which represents the relation between the normal and the shear displacements of the wall (ψ =arctan Δ_n/Δ_s) and assumes a significant role in numerical modeling of rubble stone masonry [25]. Indeed, an increase in the volume of stone specimens can be observed during the test because, after cracking and sliding, the two sides of the cracks do not match. For this reason, the dilatancy of stone masonry is mostly controlled by the joint roughness, as already observed for rock joints [29]. Indeed, the dilatancy increases with the irregularity of the crack surfaces and tends to be stronger in rubble stone masonry than in brick masonry [8]. As pointed out by [30], dilatancy in masonry panels causes a significant increase in the shear strength when they are subjected to confinement loads.

To quantify the shear strength parameters of horizontal bed joints in rubble stone masonry, triplet tests were performed at the laboratory LPMS of the University of L'Aquila on two stone masonry samples measuring about 0.50 m in length, 0.50 m in height and 0.30 m in thickness. Samples were prepared using the original limestone units and the ancient constructive technique recognized in most of the monumental buildings of L'Aquila. Irregular stone elements of calcareous nature and with a characteristic size ranging from 80 mm to 150 mm were taken from the debris of buildings collapsed under the L'Aquila 2009 earthquake. The original mortar features of the historical masonry (characterized by a very friable behavior and a low compressive strength of about 2 MPa) were reproduced several attempts. In particular, the mortar was prepared by mixing commercial natural hydraulic lime mortars, local crushed limestone sand and local natural clay with a respective ratio of 1:2:1. Water was added to the mortar mixture until a plastic consistency was reached. The addition of natural clay to the mortar mixture produced a hydraulic lime similar to the ancient lime [31]. Wall samples were consolidated by mortar injections to preserve their integrity during the delicate movement operations.

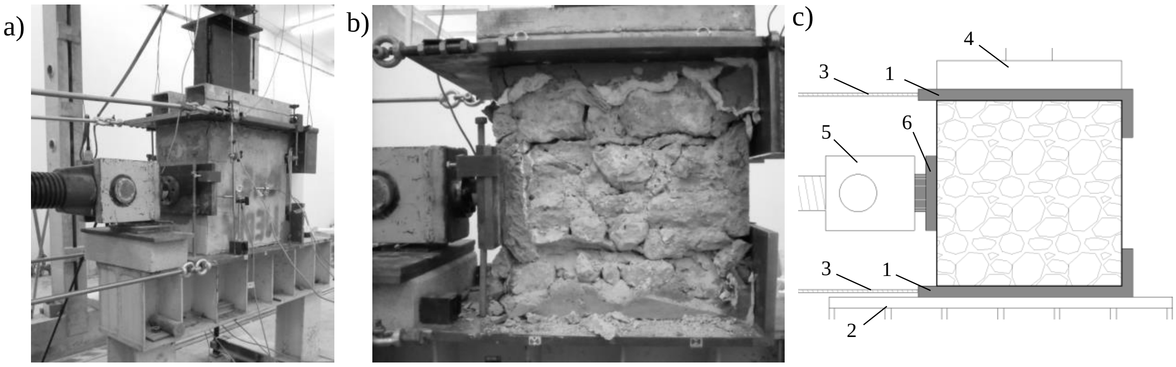

Figure 1. (**a**) Testing apparatus employed for the triplet tests carried out at the laboratory LPMS of the University of L'Aquila. (**b**) Specimen failure. (**c**) Experimental details of the test.

Here, it is relevant to say that test equipment consisted of a pair of rigid steel plates (measuring 30 mm in thickness) mounted around the masonry wall panels to simulate a shear box (see items 1 in Figure 1*c*). The bottom plate was placed on a rigid steel basement (see item 2 in Figure 1*c*). Both the top and bottom steel plates were anchored by steel bars (see item 3 in Figure 1*c*), which did not allow horizontal translations of the plates.

As far as the load system is concerned, first, a vertical actuator was used to impose an axial load to the sample (see item 4 in Figure 1*c*), reaching the average compression stress of -0.18 MPa (equal to about 1/3 of the failure stress experimentally obtained from the compression of a sample), which was kept constant for all the duration of the tests. Second, a horizontal actuator (see item 5 in Figure 1*c*) was used to introduce a shear force H at the half-height of the sample by using a lateral steel plate (see item 6 in Figure 1*c*).

Due to the boundary and loading conditions designed in the experiments, the central zone of the sample was forced to slide on the upper and lower specimen parts through two distinct shear surfaces.

Further details about the manufacture of the masonry samples, the test equipment, and the test execution are provided in [24].

Figure 1*b* shows the crack propagation occurred during the experimental test. In particular, one can clearly observe a crack concentration at the horizontal layers between the lateral plate and the two

L-shape plates. Lower amount cracks also occurred at the bottom and upper parts of the specimens. It is worth noting that a rotation of the upper part of the specimen was observed during the tests.

The mechanical response of the specimens carried out by experimental tests is described in the Section 4.

In the absence of specific standards for the testing of irregular stone masonry walls, the described test configuration aimed to reproduce the triplet test usually performed on brick masonry samples (EN1052-3, [28]). In particular, the shear stress of the specimen f_v is obtained from the equation:

$$f_v = H/(2A) \tag{1}$$

where H is the shear load and A is the cross-sectional area of the shear surface equal to 0.12 m^2 (0.40$\times$0.30 m). Since H was applied to the central part of the specimen and transferred to the upper and lower parts through the two contact surfaces, the computation of f_v considers the total area of shear surfaces equal to $2A$ (EN1052-3, [28]). For H=H_{max}, Eq. 1 provides the maximum shear stress.

When moderate normal stress is applied on the masonry panel, the friction resistance assumes the most important role for the shear characterization of the masonries also due to the negligible resistance of the mortar [21,32]. In that condition, the Coulomb criterion can be assumed for the evaluation of the shear strength of masonry walls, accurately describing only their local failure [21,33,34], by the equation:

$$f_v = f_{v0} + \mu\, \sigma \tag{2}$$

where f_{v0} is the cohesion, which represents the shear stress at zero vertical load stress, and μ is the friction coefficient.

By combining the Eq. 1 and Eq. 2, one can compute the f_{v0} value, which represents the intrinsic mechanical property of the masonry specimen.

Reliable evaluation of the f_{v0} and μ parameters are difficult to perform in case of stone masonry because they strongly depend on the asperity of the stones and may not be considered representative for all the entire masonry structure [35]. For stone units coupled with hydraulic lime mortar, f_{v0} values ranging from about 0.08 to 0.3 were experimentally measured [8,36].

In national [37] and international codes [38], μ is considered as constant and independent from the wall type and assumed equal to 0.4. Instead, experimental values of such coefficient were measured, in case of stone units coupled with hydraulic lime mortar, ranging from about 0.3 to 1.2 [8,36,39].

3. Description of the numerical model

Extensive researches on advanced numerical modeling and analysis of historic masonry structures have been carried out since some decades [40–42]. However, reliable prediction of the mechanical response of such material is still a challenge for engineers [43].

Different modeling approaches are available for the numerical simulation of the mechanical behavior of masonry structures. Actually, both the macro-models, also called continuous models, [44–48] and micro-modelling, also called discontinuous models, [30,49–51] may be adopted on the base of the different detail to which the material heterogeneity are required to be represented.

The discontinuous approach can give better results, especially when the geometry is known, but is computationally expensive for the analysis of large masonry structures since the failure zones are placed in pre-assigned weak zones, such as the mortar joints for brick masonries [52]. Instead, the continuum approach performs well in case of damage zones spread over the wall [53].

Previous researches showed that the response of masonry structures up to failure can be successfully modeled using techniques applied to concrete mechanics because both are characterized by brittle behavior [54–56].

In the present work, the in-plane compressive behavior of UnReinforced Masonry (URM) walls was investigated by using a macro-modeling approach, where the heterogeneous material is substituted with an equivalent homogeneous material. In particular, the experimental tests described in Section 2 were simulated by using Midas FEA [57]. This FE code can be used for simulating the behavior of quasi-brittle materials, such as the stone masonries, by employing the Total Strain Crack Model - TSCM [58]. The TSCM is often used for macro-modelling of masonry [45–47]. It is based on the Modified Compression Field Theory originally proposed in the multi-direction fixed crack model [59] and extended to 3D by [60]. The model is based on a smeared crack approach, where the process of cracking is obtained by "smearing" the damage on the adjacent finite element, introducing a degradation of the relevant mechanical properties [61]. The model also offers a variety of possibilities to consider the orientation of the crack, ranging from fixed single to fixed multi-directional and rotating crack approaches [62,63]. Since smeared crack modeling approaches do not require remeshing of the FE model after the occurrence of cracks or a priori definition of possible locations of cracks, they have been widely used in FE modeling [64]. The smeared crack models are practice-oriented due to the limited data required in input and, for example, was successfully adopted for brick masonry and adobe walls [65,66] and debonding problems [64,67,68].

In the present work, under the TSCM hypotheses, the fixed stress-strain concept was used, so that the axes of crack remain unchanged once the crack is activated. Furthermore, both the lateral crack and the confinement effect were considered. The system of non-linear equations used a secant stiffness matrix and was solved by the Initial stiffness incremental method.

The compression behavior of the masonry was modeled by the constitutive law suggested in [69], characterized by a parabolic hardening path and a parabolic exponential softening branch after the peak of resistance (Figure 2*a*). The tensile behavior was instead modeled by the Thorenfeldt's law [70] characterized by a linear hardening branch followed by a nonlinear softening branch (Figure 2*b*).

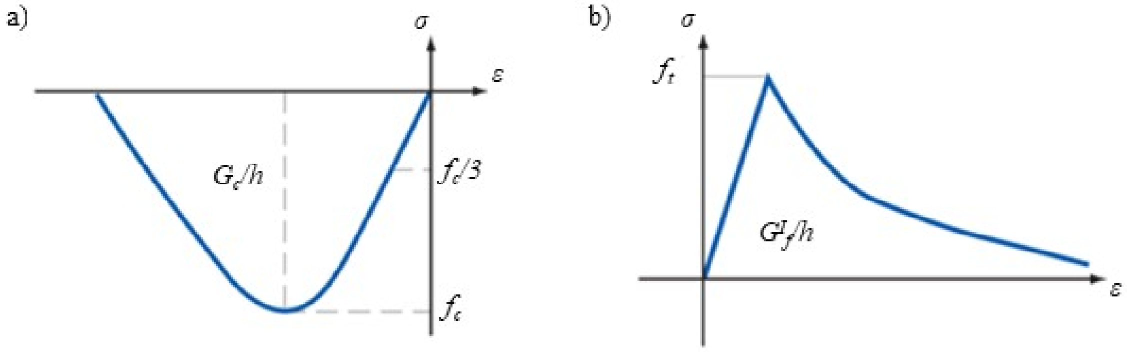

Figure 2. Stress-strain constitutive relations: (**a**) masonry uniaxial compression. (**b**) masonry uniaxial tension

The stone masonry panel was modeled by the FE macro-model M1 illustrated in Figure 3*a*. The M1 consists of a single block of homogeneous material characterized by a hexahedral mesh with a size of 50 mm. In particular, in a continuum modeling approach, the mesh size should be larger than the size of the aggregates and other dominant micro-structure features. However, authors decided to use a mesh size which was as close as possible to the real stone size. This because of the convergence issues of the analyses that would lead to lower reliability of the numerical results.

The two L-shape plates, placed at the lower and the upper parts of the specimen (see items 1 and 2 in Figure 3*a*), were modeled as tetrahedral elements and were assumed to be elastic. The same assumption was adopted also for the lateral plate (see item 3 in Figure 3*a*) used to transfer the horizontal displacement to the central zone of the sample.

As far as the load is concerned, two different loading steps were applied to the panel aiming to reproduce the same condition of the experimental tests: (i) a constant vertical compression stress of 0.18 MPa on the upper L-shape plate (see item 2 in Figure 3*a*) to have a uniform distribution of the vertical load and (ii) a horizontal displacement, gradually increasing from 0 mm to 20 mm, transferred by the lateral plate to have the sliding of the central zone of the sample.

As far as the constraint system is concerned, the vertical translations together with the rotations perpendicular to the normal plate directions were fixed for all the bottom mesh nodes. Furthermore, only horizontal translations were fixed for the outermost mesh points of the two L-shape plates. The top of the sample was left free to move in the vertical direction like in the experimental tests. That constraint system allowed to reproduce the same boundary of the experimental tests. Details of the constraint system adopted in the simulation are illustrated in Figure 3*b*.

Since small numbers of iterations and steps used for the numerical analyses may affect the quality of the calculated responses, a huge number of iterations and steps were assumed for the analyses. In particular, 150 iterations and 200 steps, which correspond to an increment of 0.1 mm per step, were assumed to solve the nonlinear equation system by using the incremental Newton-Raphson method.

4. Simulating the experimental tests

4.1. Calibration of the material parameters

The composite nature of the masonry makes it difficult to assign material properties, which depend on many factors as described above. For this reason, the first important part of the work consisted of calibrating the mechanical parameters in order to reproduce the mechanical behavior observed during experimental tests.

The masonry mechanical properties required by the model were the normal elasticity modulus E, the shear modulus G, the compressive strength f_c, the tensile strength f_t and the compressive and tensile energy fractures, G_{f_c} and G_f, respectively. The values of f_c and f_t were assumed equal to those ones obtained experimentally in [24]. The normal elasticity modulus E and the shear modulus G were defined by the best fitting of both the H-d_x and f_v-ε_v experimental curves recorded during the tests performed in [24]. On the other hand, it was necessary to calibrate the values for G_{f_c} and G_f to model the inelastic behaviour of the URM. In particular, the G_{f_c}/h and G_f/h ratios represent the the area under the stress-strain ($\sigma - \varepsilon$) diagrams of Figure 2, where h represents the crack bandwidth and it can be assumed equal to the average mesh size adopted in the FE model [57,71]. However, any experimental investigation presents in the literature allows a reliable characterization of both the G_{f_c} and G_{fI} for stone masonries. Empirical formulations can be applied for the estimation of such parameters:

$$G_{f_c} = 15 + 0.43\, f_c - 0.0036\, f_c^2 \tag{3}$$

$$G_{fI} = 0.025\, (2\, f_t)^{0.7} \tag{4}$$

One compute a value of 15.2 N/mm for G_{f_c} by using the Eq. 3 and a value of 0.0075 N/mm for G_{f_c} by using the Eq. 4. Such values were computed with the f_c and f_t values listed in Table 1. However, such equations were proposed for brick masonries [72] by modifying the formulation originally proposed for the concrete material [73]. In case of stone masonries, Eq. 3 tends to overestimate the G_{f_c} value. Indeed, for example, the value assumed for G_{f_c} in the numerical analyses carried out for the Camponeschi Palace [64], which is an historical stone masonry building located in L'Aquila, was assumed equal to 9 N/mm. Values of 3 N/mm were instead estimated for G_{f_c} in case of tuff masonry material [61,74,75].

On the contrary, the G_{fI} value obtained by the Eq. 4 slightly underestimates the values presented in the literature [52,64]. Sensitivity analyses on such mechanical parameters would deserve a deeper investigation and should be considered in future studies.

Table 1 shows the masonry parameters obtained by the described calibration procedure. It should be noted that the ratio $E/G = 2.2$ is close to the value provided by the Italian Building Code [37] for irregular stone masonries assumed equal to 3.

Table 1. Mechanical parameters calibrated for the masonry panel under shear-compression.

E [MPa]	G [MPa]	f_c [MPa]	G_{fc} [N/mm]	f_t [MPa]	G_{fI} [N/mm]
100	45	0.7	15.2	0.09	0.0075

Figure 3c shows the best fitting of the experimental curves. In particular, the grey area represents the dispersion between the lower and the upper response curves measured in the two experimental tests, whereas the black curve concerns the numerical simulation. No extensive literature reports regard triplet test on stone masonry specimens, since the test is commonly employed only for brick masonries. However, the results of both the experiment and simulation presented in this paper are in line with the literature results obtained for the same masonry type and same materials [8,76]. Here, the maximum shear stress f_v was almost equal to 0.26 MPa, whereas the shear stresses f_v computed in [8,76] were ranging from 0.33 MPa to 0.44 MPa, obtained for vertical compression stress similar to the one applied for the present case. The slight difference is related to the classic scattering issue that is typical for stone masonry, as described in Section 1.

In the rest of the paper, the numerical curve of Figure 3c is taken as the reference curve for the H-dx plots.

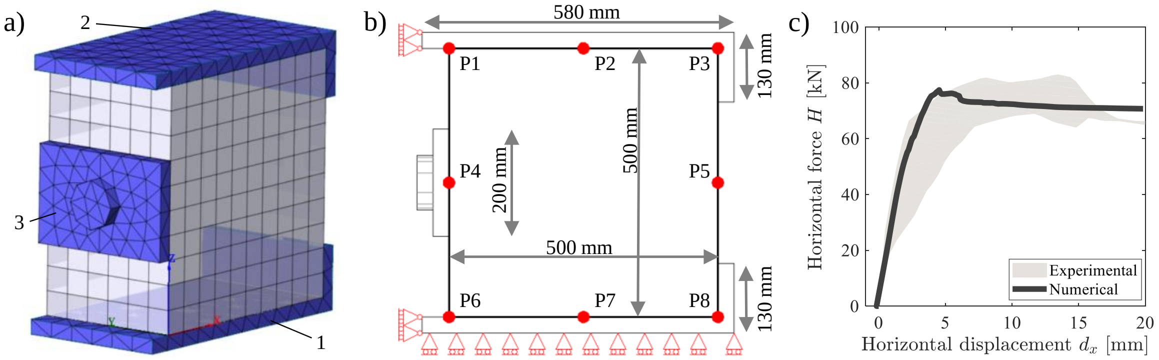

Figure 3. (**a**) Visualization of the M1 macro-model. (**b**) Scheme adopted in the test. (**c**) Best fitting of the H-d_x experimental response.

4.2. *Numerical assessment of the shear mechanic parameters*

The experimental tests carried out in [24] measured the relation H-d_x (Figure 3c) up to the failure of the URM sample, whereas the relation f_v-ε_v was evaluated only in the elastic phase (up to 1/3 of the shear strength). However, to better investigate the mechanical behavior of the URM specimen under triplet test, it is important to measure also other parameters. In this work, the displacement of eight points (from P1 to P8) placed on the face of the panel (see Figure 3b) were monitored during the simulation aiming to compute the shear displacement Δ_s, the normal displacement Δ_n, the horizontal strain ε_h and the vertical strain ε_v. In particular, ε_h and ε_v were computed for both the middle and lateral parts (left, right, top and bottom) of the sample, as follows:

$$\varepsilon_{h,middle} = -(d_{x,P4} - dx_{P5})/\ell \tag{5}$$

$$\varepsilon_{h,top} = -(d_{x,P1} - dx_{P3})/\ell \tag{6}$$

$$\varepsilon_{h,bottom} = -(d_{x,P6} - dx_{P8})/\ell \tag{7}$$

$$\varepsilon_{v,middle} = (d_{z,P2} - dz_{P7})/\ell \tag{8}$$

$$\varepsilon_{v,right} = (d_{z,P3} - dz_{P8})/\ell \tag{9}$$

$$\varepsilon_{v,left} = (d_{z,P1} - dz_{P6})/\ell \tag{10}$$

$$\Delta_s = d_{x,P5} - (d_{x,P3} + d_{x,P8})/2 \tag{11}$$

$$\Delta_n = d_{z,P3} \tag{12}$$

were ℓ is the length between two points, equal to 500 mm, d_x and d_z are the horizontal and the vertical displacements of the eight points placed on the face of the panel.

Results of the numerical simulations are illustrated in Figures 4$a - f$. Plots indicate the achievement of the maximum shear stress $f_{v,MAX}$ by the "x" marker and called MSP label (Maximum Stress Point) in the following. Instead, when the achievement of the maximum normal and shear displacements occur at the same point, $\Delta_{n,MAX} \equiv \Delta_{s,MAX}$, the "o" marker and the MDP label (Maximum Displacement Point) are used in the paper.

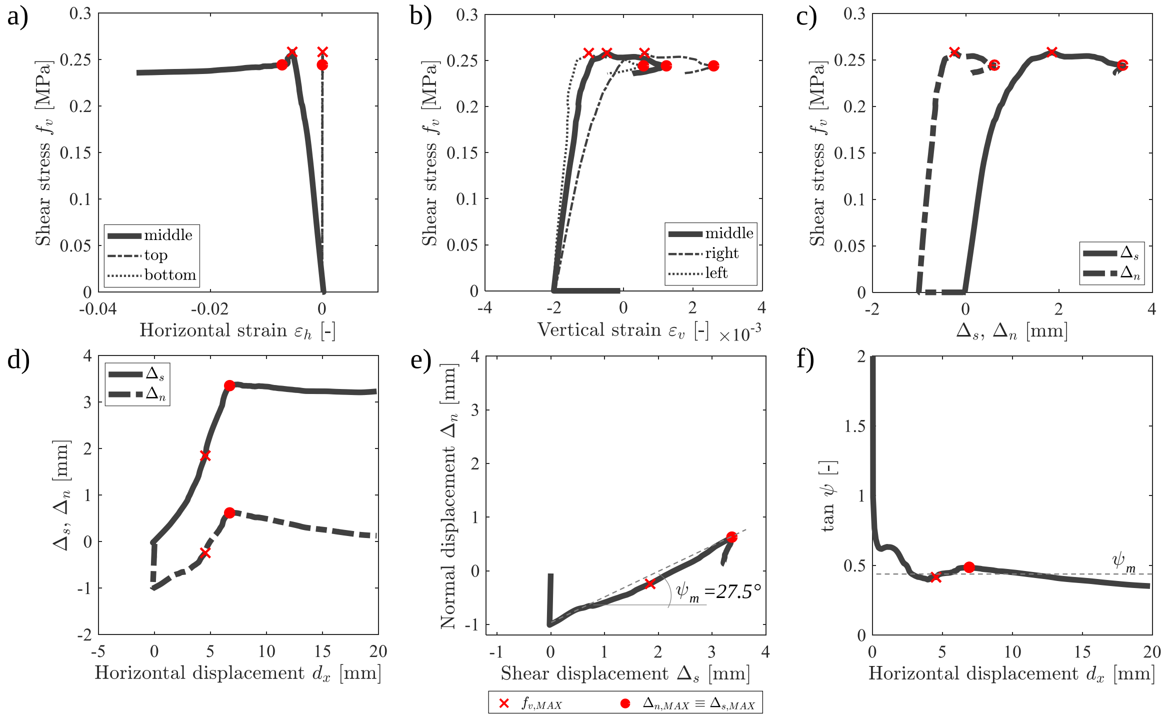

Figure 4. Numerical results obtained for the M1 model.

In detail, Figure 4a shows the relation between f_v and the horizontal strains ε_h computed for the three parts of the sample: middle, top, and bottom. In particular, one can see that the strain values computed for the top and the bottom parts of the specimen assume a constant value almost equal to zero because of the nearness of the L-shape plates that constrain the horizontal displacement of the specimen. For the middle part of the sample, an initial, almost linear branch is first recognized up to the MSP, then the mechanical response of the masonry is characterized by a gradual reduction in f_v up to MDP, after which a large increase in ε_h is observed for constant residual value of f_v. In the rest of

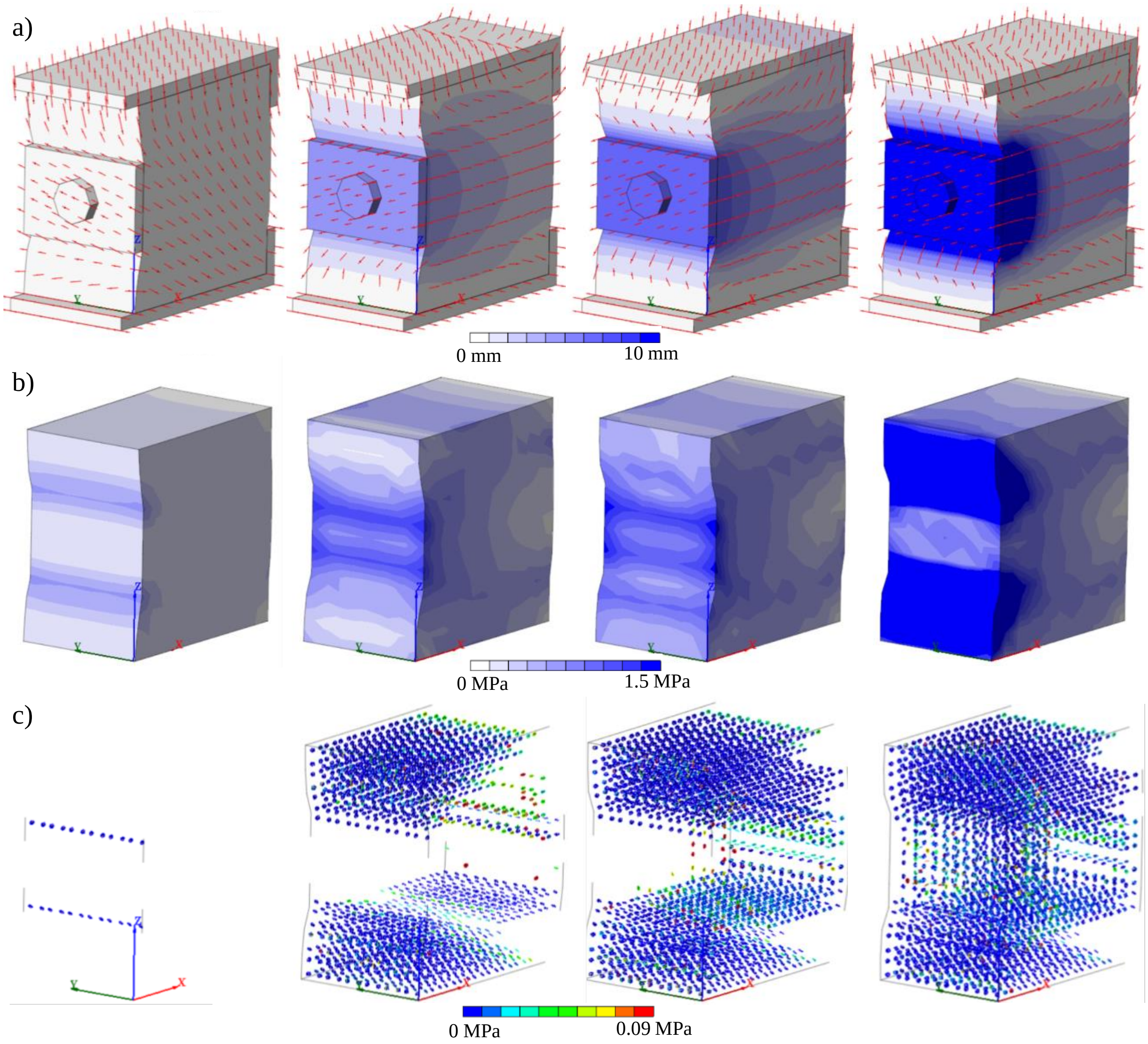

Figure 5. Masonry specimen for incremental values of the displacement d_x corresponding to the elastic phase (1 mm), maximum shear stress (4.5 mm), maximum shear and normal displacement (6.9 mm) and the end of the test (20mm) and illustrated in terms of: (**a**) displacement field (Dxyz plots). (**b**) Stress field (Von Mises plots). (**c**) Evolution of the cracking pattern.

the paper, the numerical curve of the middle part of the sample represented in Figure 4*a* is taken as the reference curve for the f_v-ε_h plots.

Figure 4*b* shows the vertical strains ε_v computed for three parts of the sample: middle, right and left. In particular, for all three curves, one can observe compressive values (negative) equal to -0.002 MPa for f_v = 0 Mpa. This is due to the compressive load applied to the upper L-shape plate in the first loading step. Then, one can see a gradual increase in ε_v for all three curves up to the MSP, after which a large increase in ε_v is observed for a constant residual value of f_v up the MDP. After the achievement of the MDP, one can observe that f_v continues to decrease because the specimen is gradually damaged now allowing the transmission of the force H to the masonry specimen, Furthermore, after the achievement of the MDP, one can also observe a decrease in the ε_v value because, at that point, the specimen is almost completely collapsed and cannot longer resist to the vertical compression pressure σ applied on the upper plate. Hence, the specimen tends to return to the initial configuration of the uncompressed statement.

doi:10.20944/preprints202002.0226.v1

Analyzing the differences between three curves of Figure 4*b*, one can see that the right and left parts of the specimen are characterized by different values of ε_v as compared to the middle part. This is due to the rotation of the specimen that also occurred in the experimental test.

Figure 4*c* shows the correlation between shear stress f_v and both normal and shear displacements, Δ_n and Δ_s. In general, the trends and the comments of Figure 4*b* are transferable for the Figure 4*c*.

Figure 4*d* shows the variation of both Δ_n and Δ_n as function of the displacement of the lateral plate d_x. In particular, one can observe a gradual decrease of both Δ_n and Δ_n when the MSP is reached.

As discussed in the Section 2, it is known from the literature that quasi-brittle materials show an increase in volume when undergoing inelastic shear deformations. This phenomenon depends on both the confinement pressure and the dilatancy angle ψ. The dilatancy ψ represents the relation between the vertical and the horizontal displacement of the wall (ψ =arctan Δ_n/Δ_s). Figure 4*e* shows the relation between Δ_s and Δ_n computed for the specimen, allowing to graphically estimate the mean dilatancy angle, equal to 27.5 ^{o}. That curve is taken as the reference curve for the Δ_n-Δ_s plots in the rest of the paper.

Finally, Figure 4f shows the relation between tan ψ and the displacement of the lateral plate d_x. One can observe that the tan ψ assumes high value during the compressive loading phase (d_x=0) and an almost constant value equal to 0.48 during the application of the lateral displacement d_x. Results are in line with the results of Van der Pluijm [77], who experimentally established values of tan ψ, ranging from 0.2 to 0.7 for low confinement pressures, highlighting the strong influence of the confinement on the estimation of ψ.

To better understand the variation of both the displacement and stress fields during the triplet test, Figures 5*a*, *b* show the plots corresponding to incremental values of the displacement d_x imposed at the lateral plate. In particular, plots of Figures 5*a*, *b* are referred to d_x equal to 1 mm, 4.5 mm, 6.9 mm, and 20 mm, ensuring to observe the mechanical behavior at the elastic phase (pre-peak), maximum shear stress, maximum shear and normal displacements, and the end of the test. Displacement field are illustrated in Figure 5*a*, whereas the stress field (Von Mises plots) is illustrated in Figure 5*b*.

Furthermore, Figure 5*c* shows the evolution of the cracking pattern of the masonry sample for incremental values of d_x in terms of Gauss point-occurrence, indicating whether a tension cut-off limit is exceeded at an integration point. In particular, one can see that the upper and lower parts of the specimen are characterized by larger damage level as compared to the central part of the specimen. In detail, crack concentration occurs at the horizontal layer between the lateral plate and the two L-shape plates and the corners places. Definitely, the cracking pattern observed in Figure 5*c* highlights that the simplified numerical modeling which considers all nonlinear behaviour of the masonry sample concentrated on the sliding surfaces, while keeping the three parts of the specimen as elastic, may produce incorrect results.

4.2.1. Confinement effect

The confinement effect, which can take place between two contact surfaces, was considered in the analyses by assuming the Selby-Vecchio law [60] in the material properties, as discussed in the Section 2. Results presented in the follows (Figures 6 and 7) describe the variation of the mechanical properties of the masonry sample by varying the value of the confinement pressure, assumed equal to -0.18 MPa (σ_0 case), -0.09 MPa (0.5 σ_0 case) and -0.36 MPa (2 σ_0 case).

Results of Figure 6 highlight that the confinement level affects the strength of the specimen. Moreover, for the case of low confinement pressure (0.5 σ_0 case), one can observe a hardening behavior of the response, whereas for the other two cases a softening behavior is observed. Furthermore, it is worth noting that, for the case of 0.5 σ_0, the shear displacement and the normal displacement occur at the same value of d_x, as already observed for the σ_0 case. On the contrary, for the case of 2 σ_0, one can observe that $\Delta_{n,MAX}$ and $\Delta_{s,MAX}$ occur in two different phases. In particular, in 2 σ_0 case, $\Delta_{n,MAX}$ and $\Delta_{n,MAX}$ occur before and after the achievement of the MSP, respectively.

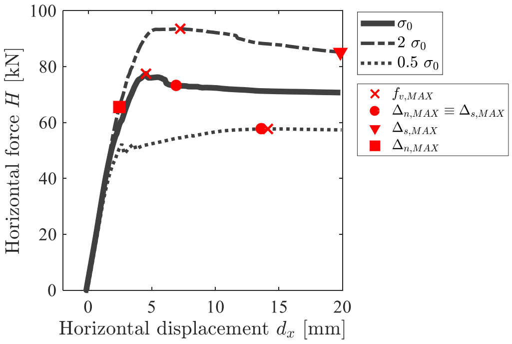

Figure 6. Confinement effect in the horizontal displacement-horizontal force plot.

Figure 7*a* shows the relation between the normal displacement Δ_n and the shear stress f_v. It is worth noting that no considerable lifting of the masonry sample can be observed in case of high confinement pressure (2 σ_0 case). Indeed, after the initial compressive phase that leads to normal displacement equal to -2 mm, a slight lifting of the sample is observed up to $f_v = 0.22$ MPa, for which is computed the maximum value of Δ_n. After that point, the sample continues to be compressed, showing a decrease in Δ_n. For the case of low confinement pressure (0.5 σ_0 case) one can see that the MSP coincides with the MDP and they occur at the end of the test.

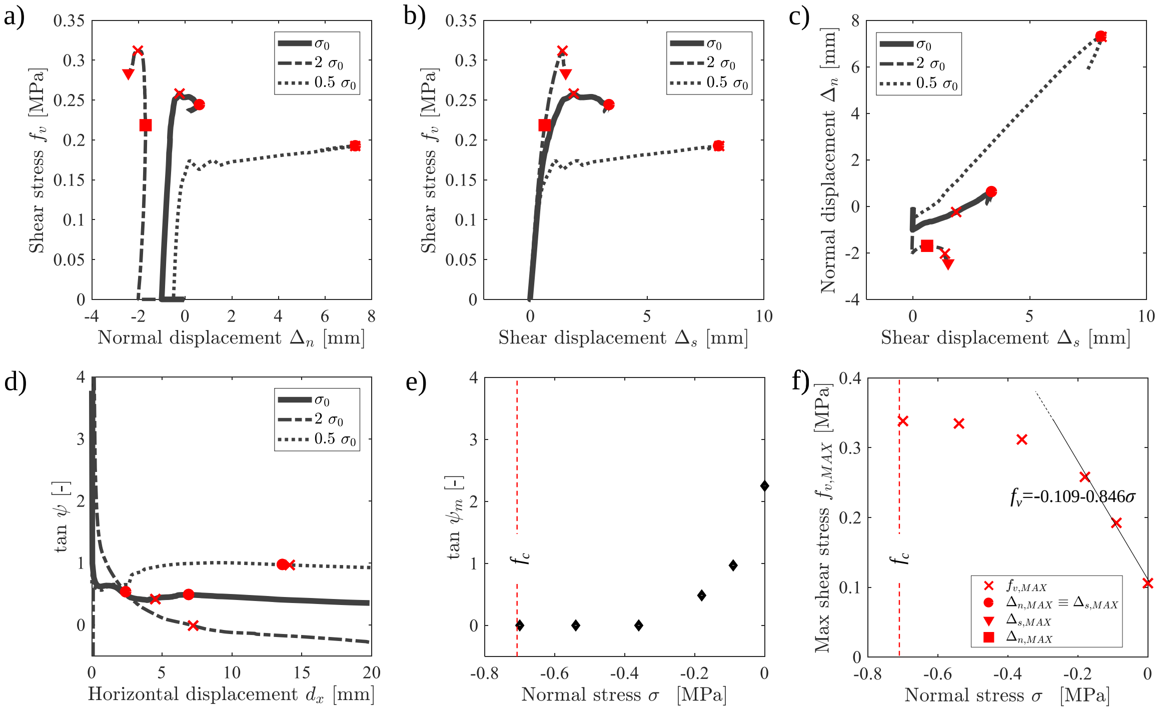

Figure 7. Investigation of the shear mechanical properties of the masonry sample by varying the confinement pressure respect to the central value σ_0 equal to -0.18 MPa.

Figure 7*b* shows the relation between the shear displacement Δ_s and the shear stress f_v. For all the three curves, the achievement of the maximum value of the shear displacement $\Delta_{s,MAX}$ is observed after the achievement of the MSP. Moreover, $\Delta_{s,MAX}$ occur at the end of the test only for the case of high confinement pressure, as already clearly observed in Figure 6.

Figure 7*c* shows the relation between Δ_s and Δ_n computed for the specimen allowing to graphically estimate the mean dilatancy angle ψ_m. Values of *tan* ψ are analysed in Figure 7*d* as function of the lateral displacement d_x. In that figure, one can see that, after the initial phase (d_x almost equal to 0), the dilatancy tends to be constant. Moreover, the higher confinement pressure, the higher $tan\ \psi$ value is, with a null value of $tan\ \psi$ in the 2 σ_0 case.

Additional analyses (Figure 7d, e) were carried out also assuming values of σ equal to 0 MPa, -0.54 MPa and -0.7 MPa to better understand the variation of both tan ψ and $f_{v,MAX}$ as function of the confinement pressure. In particular, the results of Figure 7d show that tan ψ is ranging from 0 to 2.25 following an exponential law. Figure 7f allows to define the limit strength domain of masonry and to estimate values of the cohesion f_{v0} and the coefficient of friction μ. In particular, f_{v0} and μ were computed equal to -0.109 MPa and -0.846 MPa, respectively, by assuming a linear regression of the results obtained for σ_0 equal to 0 MPa, -0.18 MPa and -0.36 MPa.

4.2.2. Bond effect at the masonry-plates interface

Analyses carried out in Sections 4.2 and 4.2.1 regarded the hypotheses of perfect bond (PB) behavior at the specimen-plate interfaces. However, in the experimental tests, the masonry specimens could move along the horizontal direction, whereas only the horizontal displacement of the L-shape plates was constrained. Here, to lies a sliding at the specimen-plates interface, a weak bond (WB) hypotheses was assumed in the FE model. In particular, contact plane elements were introduced by assuming the Coulomb friction nonlinear law [57] with values of 0.05 MPa for the cohesion c, 30^o for the internal friction angle ϕ, 80 N/mm^3 and 35 N/mm^3 for the normal and the tangential stiffness k_n and k_t, respectively.

Results presented in the following (Figures 8) describe the variation of the mechanical properties of the masonry sample by varying the bond behavior at the sample-plates interfaces.

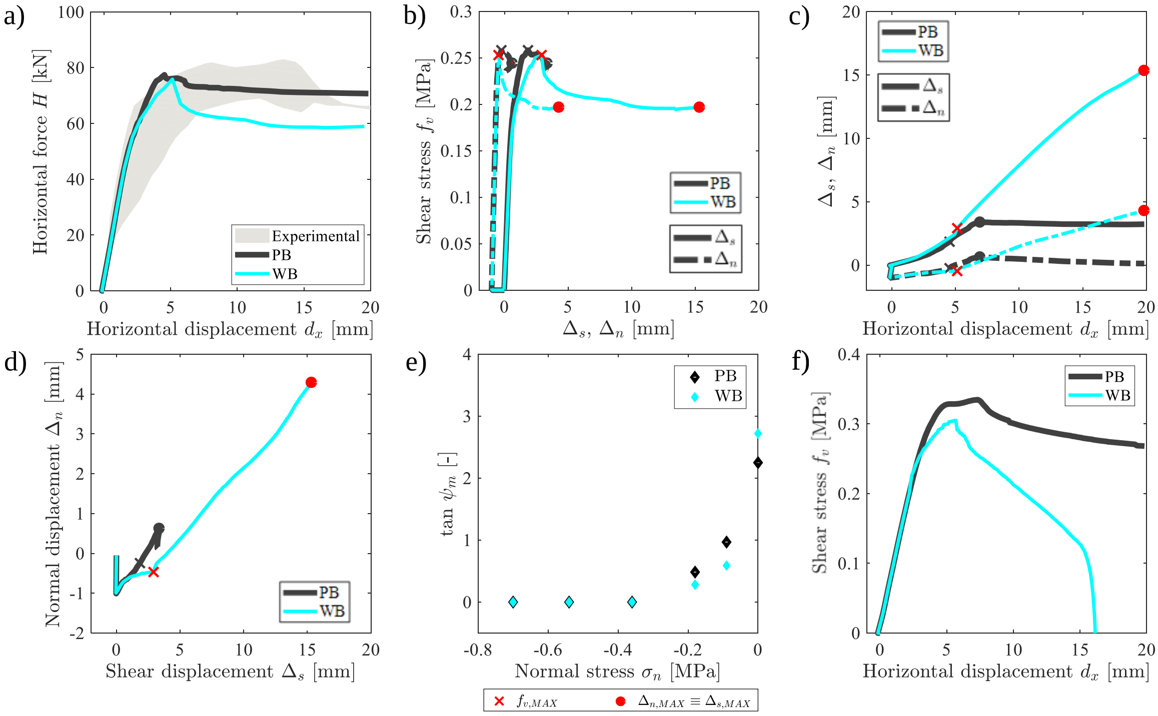

Figure 8. Comparison of the numerical results between the cases of two different bond behaviors at the masonry-plates interfaces: perfect bond (PB) and weak bond (WB) behavior.

Figure 8a shows that the bond behavior has no effect in the first branch of the H-d_x plot and has a slight effect on the maximum shear load (about 2%). On the contrary, a larger difference in terms of load-bearing capacity for large displacement d_x is observed between the WB and the PB cases. Indeed, by measuring H at d_x=20 mm one can compute a load decrease of 17 % by comparing the PB (71 kN) and WB (59 kN) cases. Moreover, in the WB case, one can observe, after the achievement of about 60 kN of the horizontal force, a higher decrease in the slope of the response curve as compared to the

doi:10.20944/preprints202002.0226.v1

PB case. This difference means that the WB hypothesis leads to an early non-linear phase of the wall material. It is worth noting that the experimental response shows the same decrease in the slope of the mechanical response, even more pronounced.

Figure 8*b* shows the relation between both the normal and shear displacements with the shear stress f_v. In particular, strong differences can be observed in terms of the MDP value, which is higher in the WB case as compared to the PB case.

Figure 8*c* shows the variation of both Δ_n and Δ_n as function of the lateral displacement d_x. The plot clearly highlights the higher deformation capacity of the masonry sample in the WB case as compared to the PB case. Indeed, for the PB case, one can see that Δ_n and Δ_n assume constant values after a certain value of d_x (almost equal to 6 mm), whereas a gradual increasing in both Δ_n and Δ_n up to the end of the test is observed for the WB case.

Figure 8*d* shows the relation between Δ_s and Δ_n computed for the specimen. In particular, one can see that the dilatancy angle is higher for the PB case as compared to the WB case.

Results of Figure 8*e* show the particular variation of the trend of tan ψ_m function of the normal stress σ by assuming PB and WB hypotheses.

A further analysis is carried out to investigate the effect of the boundary condition on the mechanical response of the masonry subjected to high confinement pressure. Figure 8*f* shows the $f_v - d_x$ plot for high confinement pressure (2 σ_0 case). In particular, one can compute a decrease in the shear strength of about 11 % by comparing the PB case (0.350 MPa) and the WB case (0.312 MPa). Moreover, one can note a total decay of the shear stress for the WB case, whereas a good bearing-load can be observed for the PB case, which is characterized by a decrease in f_v of about 20 % as compared to the peak value. Definitively, by comparing the response of Figure 8*a* and Figure 8*f*, one can say that the higher the confinement pressure, the higher the influence of bond behavior on the mechanical response.

Finally, Figure 9 shows the effect of the bond behavior at the masonry-plate interfaces on the displacement and stress fields, and the fracture propagation in case of high confinement pressure (2 σ_0). Plots concern different values of the displacement d_x, equal to 4 mm and 16 mm. In particular, one can see clear differences in the sample deformation by assuming the PB hypothesis (Figure 9*a*) and the WB hypothesis (Figure 9*b*). Differences in terms of the Von Mises stress for the PB and WB hypotheses are investigated in Figures 9*c*, *d*. As far as the fracture propagation is concerned, first, one can see that the WB case (Figure 9*e*) leads to a higher cracking amount as compared to the PB case (Figure 9*f*). Second, it is worth noting that one can observe different cracking patterns by assuming different confinement pressure and the same bond behavior hypothesis. Indeed, under the PB hypothesis, the damage pattern on the sample for the 2 σ_0 case (Figure 9*e*) concerns its lateral parts, whereas one can see cracks concentration at the lower and bottom parts of the sample for the σ_0 case (Figure 5*c*).

Definitely, by comparing both the mechanical response and the propagation failure on the masonry walls of the experimental test presented in this paper, the WB case can be considered most realistic respect to the PB case.

5. Conclusions

The numerical assessment of the shear mechanical parameters on unreinforced stone masonry walls under triplet test configuration was carried out in the present work.

First, the paper introduces experimental tests carried out at the laboratory LPMS of the University of L'Aquila on several stone masonry samples prepared by using the original limestone units and the ancient constructive technique recognized in most of the monumental buildings of L'Aquila.

Second, the tests were numerically simulated by using a macro-model under the Total Strain Crack assumption, in order to determine the dilatancy, displacement, deformation, and strength of the sample. The results showed a good agreement between experiments and numerical simulations in both the mechanical behavior and the damage evolution on the masonry sample. Then, the effect of the confinement pressure and the bond behavior at the masonry-plate interfaces were also investigated.

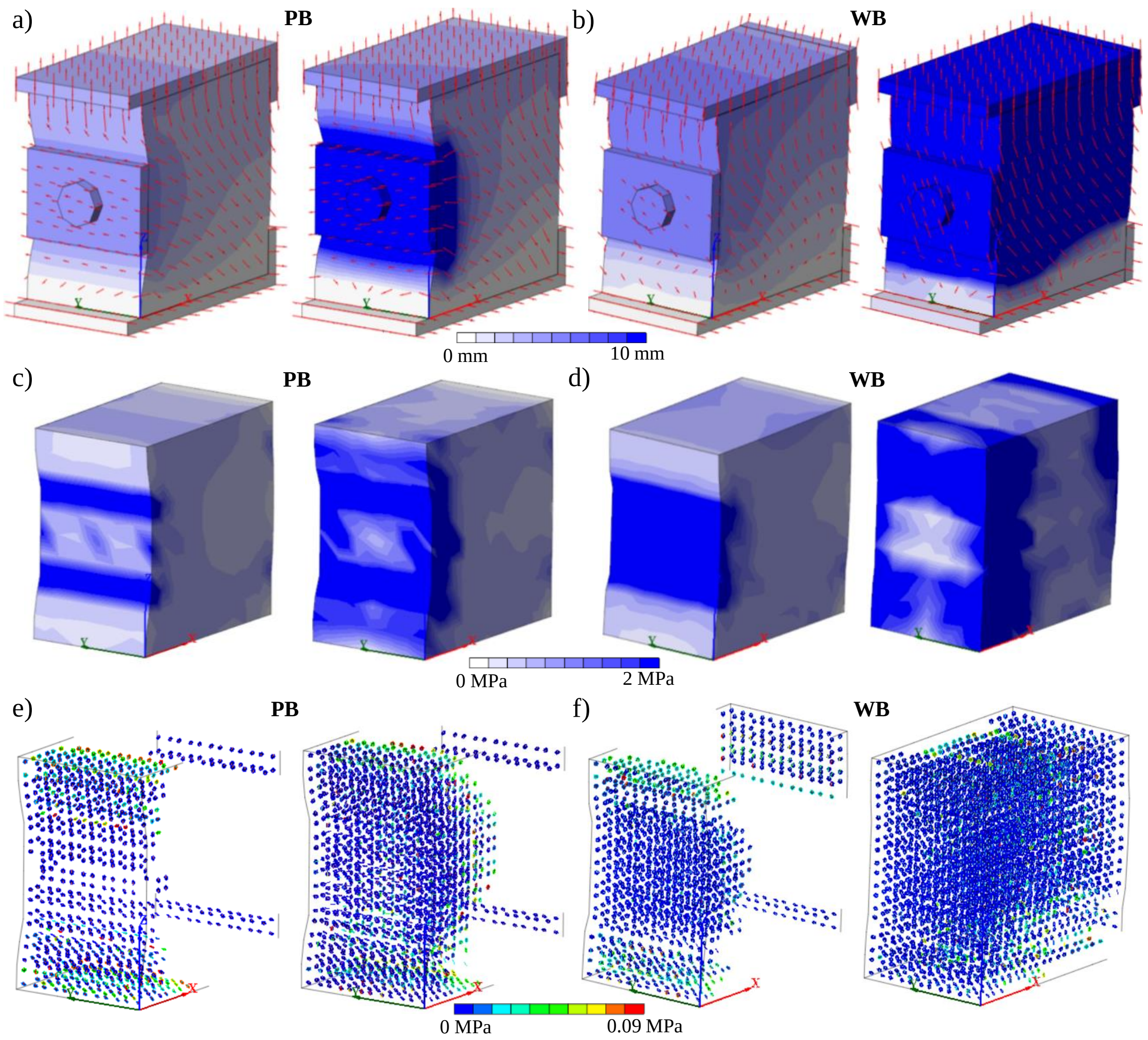

Figure 9. Results obtained for high confinement pressure (2 σ_0 case) and plotted for two different steps (d_x=4.5 mm and d_x=16 mm) by varying the the bond behavior at the masonry-plate interfaces (Perfect Bond (PB) and Weak Bond (WB) hypothesis). Imagines are illustrated in terms of: (**a**,**b**) displacement field (Dxyz plots). (**c**,**d**) Stress field (Von Mises plots). (**e**,**f**) Evolution of the cracking pattern.

In particular, as far as the confinement pressure is concerned, simulations showed that it highly affects the shear strength and the dilatancy of the sample. In addition, it was found that the shear and normal maximum displacements do not occur at the same time when a high level of the confinement pressure is applied, unlike the lower confinement pressure cases.

As far as the bond behavior is concerned, simulations showed that it has a strong effect on the load-bearing capacity for large lateral displacements imposed at the masonry sample. Moreover, the bond behavior has a slight effect in terms of the maximum shear stress and also affect the begin of the non-linear phase of the wall material.

no influence on the first part of the test (elastic field). These effects are even more evident by increasing the confinement pressure on the masonry sample.

The damage evolution on the unreinforced stone masonry sample depends to both the confinement pressure and the bond behavior, as highlighted by observing the evolution of the cracking pattern. In case of a moderate level of confinement pressure, possible failure can occur at the upper and the lower parts of the sample, and not only at the horizontal layer between the lateral plate and the two L-shape plates. Instead, in case of high confinement pressure, the cracking mainly occurs at the lateral part of the sample (close to the lateral plate used to apply the shear force to the sample). Finally, the weak bond behavior leads to a more uniform cracking as compared to the perfect bond behavior case. These results highlight that a simplified numerical model, which considers all nonlinear behavior of the masonry sample concentrated on the sliding surfaces (while keeping the three parts of the specimen as elastic) may produce incorrect results.

Acknowledgments: The Ph.D. scholarship of the first author was co-financed by the Project “2014-2020 PON" (CCI 2014EN16M2OP005).

Conflicts of Interest: The authors declare no conflict of interest. The funders had no role in the design of the study; in the collection, analyses, or interpretation of data; in the writing of the manuscript, or in the decision to publish the results.

References

1. Brandonisio, G.; Lucibello, G.; Mele, E.; De Luca, A. Damage and performance evaluation of masonry churches in the 2009 L’Aquila earthquake. *Engineering Failure Analysis* **2013**, *34*, 693–714.
2. Milani, G.; Valente, M. Failure analysis of seven masonry churches severely damaged during the 2012 Emilia-Romagna (Italy) earthquake: non-linear dynamic analyses vs conventional static approaches. *Engineering Failure Analysis* **2015**, *54*, 13–56.
3. Azzaro, R.; Tertulliani, A.; Bernardini, F.; Camassi, R.; Del Mese, S.; Ercolani, E.; Graziani, L.; Locati, M.; Maramai, A.; Pessina, V.; others. The 24 August 2016 Amatrice earthquake: macroseismic survey in the damage area and EMS intensity assessment. *Annals of Geophysics* **2016**.
4. Tinti, E.; Scognamiglio, L.; Michelini, A.; Cocco, M. Slip heterogeneity and directivity of the ML 6.0, 2016, Amatrice earthquake estimated with rapid finite-fault inversion. *Geophysical Research Letters* **2016**, *43*.
5. Penna, A.; Calderini, C.; Sorrentino, L.; Carocci, C.F.; Cescatti, E.; Sisti, R.; Borri, A.; Modena, C.; Prota, A. Damage to churches in the 2016 central Italy earthquakes. *Bulletin of Earthquake Engineering* **2019**, pp. 1–28.
6. Bosiljkov, V.; Page, A.; BOKAN, B.V. Performance based studies of in-plane loaded unreinforced masonry walls **2003**.
7. Vasconcelos, G.; Lourenço, P. Experimental characterization of stone masonry in shear and compression. *Construction and Building Materials* **2009**, *23*, 3337–3345.
8. Milosevic, J.; Gago, A.S.; Lopes, M.; Bento, R. Experimental assessment of shear strength parameters on rubble stone masonry specimens. *Construction and Building Materials* **2013**, *47*, 1372–1380.
9. Marino, M.; Neri, F.; De Maria, A.; Borri, A. Experimental data of friction coefficient for some types of masonry and its correlation with an Index of Quality Masonry (IQM). Proceedings of the 2nd European conference on earthquake engineering and seismology, Instanbul, 2014, pp. 25–29.
10. Borri, A.; De Maria, A. Indice di Qualità Muraria (IQM): correlazione con le caratteristiche meccaniche e livelli di conoscenza. *Progettazione Sismica* **2015**.
11. Corradi, M.; Borri, A.; Vignoli, A. Experimental evaluation of in-plane shear behaviour of masonry walls retrofitted using conventional and innovative methods. *Masonry International* **2008**, *21*, 29.
12. Tomazevic, M. The influence of rigidity of floors on the seismic resistance of of old masonry buildings: shaking-table tests of stone-masonry houses : summary report. **1992**.
13. Modena, C.; Bettio, C. Experimental characterisation and modelling of injected and jacketed masonry walls. *In Proceedings of Italian-French Symposium Strengthening and Repair of Structures in Seismic Area, Nizza, France* **1994**, p. 273–282.
14. Modena, C. Interpretazione dei risultati ottenuti dalle prove in sito nell’ambito delle tre convenzioni con gli istituti di ricerca di Firenze e Milano e modellazione del comportamento strutturale dei componenti rinforzati. *Convenzione di ricerca tra la Regione Toscana e il Dipartimento di Costruzioni e Trasporti dell’Università degli Studi di Padova* **1999**.
15. Corradi, M.; Borri, A.; Vignoli, A. Experimental study on the determination of strength of masonry walls. *Construction and building materials* **2003**, *17*, 325–337.
16. Borri, A.; Castori, G.; Corradi, M.; Speranzini, E. Shear behavior of unreinforced and reinforced masonry panels subjected to in situ diagonal compression tests. *Construction and Building Materials* **2011**, *25*, 4403–4414.

17. Corradi, M.; Borri, A.; Castori, G.; Sisti, R. Shear strengthening of wall panels through jacketing with cement mortar reinforced by GFRP grids. *Composites Part B: Engineering* **2014**, *64*, 33–42.
18. Magenes, G.; Penna, A.; Galasco, A.; Rota, M. Experimental characterisation of stone masonry mechanical properties. Proceedings of the 8th International Masonry Conference, 2010.
19. Silva, B.; Dalla Benetta, M.; da Porto, F.; Modena, C. Experimental assessment of in-plane behaviour of three-leaf stone masonry walls. *Construction and Building Materials* **2014**, *53*, 149–161.
20. Binda, L.; Tiraboschi, C.; Abbaneo, S. Experimental research to characterise masonry materials. *Masonry International* **1997**, *10*, 92–101.
21. Atkinson, R.; Amadei, B.; Saeb, S.; Sture, S. Response of masonry bed joints in direct shear. *Journal of Structural Engineering* **1989**, *115*, 2276–2296.
22. Lee, H.; Park, Y.; Cho, T.; You, K. Influence of asperity degradation on the mechanical behavior of rough rock joints under cyclic shear loading. *International Journal of Rock Mechanics and Mining Sciences* **2001**, *38*, 967–980.
23. Huang, T.; Chang, C.; Chao, C. Experimental and mathematical modeling for fracture of rock joint with regular asperities. *Engineering Fracture Mechanics* **2002**, *69*, 1977–1996.
24. Di Fabio, F.; Gregori, A.; Totani, M. Experimental and numerical investigations on historical masonry wall specimens tested in shear-compression configuration. *Engineering Structures and Technologies* **2015**, *7*, 177–188.
25. Vasconcelos, G. Experimental investigations on the mechanics of stone masonry: Characterization of granites and behavior of ancient masonry shear walls. PhD thesis, 2005.
26. Beattie, G.; Molyneaux, T.; Gilbert, M.; Burnett, S. Masonry shear strength under impact loading. Proc. 9th Canadian Masonry Symposium. New Brunswick. Canada, 2001.
27. Jukes, P.; Riddington, J. Review of masonry joint shear strength test methods. *Masonry International* **1997**, *11*, 37–43.
28. de Normalisation, C.E. EN 1052–3. Methods of Test for Masonry. Part 3: Determination of Initial Shear Strength, 2002.
29. Goodman, R.E. *Introduction to rock mechanics*; Vol. 2, Wiley New York, 1989.
30. Lourenço, P.J.B.B. Computational strategies for masonry structures. **1997**.
31. Sorrentino, L.; Cattari, S.; da Porto, F.; Magenes, G.; Penna, A. Seismic behaviour of ordinary masonry buildings during the 2016 central Italy earthquakes. *Bulletin of Earthquake Engineering* **2019**, *17*, 5583–5607.
32. Riddington, J.; Ghazali, M. Hypothesis for shear failure in masonry joints. *Proceedings of the Institution of Civil Engineers* **1990**, *89*, 89–102.
33. Mann, W.; Muller, H. Failure of shear-stressed masonry. An enlarged theory, tests and application to shear walls. Proc. Br. Ceram. Soc., 1982, number 30, p. 223.
34. Calvi, G.M.; Kingsley, G.R.; Magenes, G. Testing of masonry structures for seismic assessment. *Earthquake Spectra* **1996**, *12*, 145–162.
35. Dalla Benetta, M. Qualificazione di murature storiche: procedure speriementali in sito e calibrazioni in laboratorio. PhD thesis, Phd thesis in Study and Conservation of Archaeological and Architectural Heritage, University of Padova, Padova, Italy, 2012.
36. Binda, L.; Fontana, A.; Mirabella, G. Mechanical behavior and stress distribution in multiple-leaf stone walls. Proceedings of 10th international brick block masonry conference, Calgary, Canada, 1994, Vol. 45.
37. Code-NTC18, I. Norme tecniche per le costruzioni in zone sismiche. *Ministerial Decree DM* **2018**.
38. de Normalisation, C.E.; others. Eurocode 6: Design of Masonry Structures—Part 1-1: General Rules for Reinforced and Unreinforced Masonry Structures. *Comité Européen de Normalisation: Brussels, Belgium* **2005**.
39. Augenti, N.; Parisi, F. *Teoria e tecnica delle strutture in muratura. Analisi e progettazione*; Ingegneria civile, Hoepli, 2019.
40. Roca, P.; Cervera, M.; Gariup, G.; others. Structural analysis of masonry historical constructions. Classical and advanced approaches. *Archives of Computational Methods in Engineering* **2010**, *17*, 299–325.
41. Giamundo, V.; Sarhosis, V.; Lignola, G.; Sheng, Y.; Manfredi, G. Evaluation of different computational modelling strategies for the analysis of low strength masonry structures. *Engineering Structures* **2014**, *73*, 160–169.
42. Asteris, P.G.; Chronopoulos, M.; Chrysostomou, C.; Varum, H.; Plevris, V.; Kyriakides, N.; Silva, V. Seismic vulnerability assessment of historical masonry structural systems. *Engineering Structures* **2014**, *62*, 118–134.

43. Lourenço, P.B. Computations on historic masonry structures. *Progress in Structural Engineering and Materials* **2002**, *4*, 301–319.

44. Lourenço, P.B.; Rots, J.G.; Blaauwendraad, J. Continuum model for masonry: parameter estimation and validation. *Journal of structural engineering* **1998**, *124*, 642–652.

45. Faria, R.M.C.M.d. Avaliação do comportamento sísmico de barragens de betão através de um modelo de dano contínuo **1994**.

46. Faria, R.; Oliver, J.; Cervera, M. A strain-based plastic viscous-damage model for massive concrete structures. *International journal of solids and structures* **1998**, *35*, 1533–1558.

47. Silva, B.; Guedes, J.M.; Arêde, A.; Costa, A. Calibration and application of a continuum damage model on the simulation of stone masonry structures: Gondar church as a case study. *Bulletin of Earthquake Engineering* **2012**, *10*, 211–234.

48. Di Nino, S.; Luongo, A. A simple homogenized orthotropic model for in-plane analysis of regular masonry walls. *International Journal of Solids and Structures* **2019**, *167*, 156–169.

49. Lourenco, P. Computational strategies for masonry structures//Ph. D. Thesis. Delft University of Technology. Delft. The Netherlands, 1996 **1996**.

50. Costa, A.A.; Arêde, A.; Costa, A.; Guedes, J.; Silva, B. Experimental testing, numerical modelling and seismic strengthening of traditional stone masonry: comprehensive study of a real Azorian pier. *Bulletin of Earthquake Engineering* **2012**, *10*, 135–159.

51. Bolhassani, M.; Hamid, A.A.; Lau, A.C.; Moon, F. Simplified micro modeling of partially grouted masonry assemblages. *Construction and Building Materials* **2015**, *83*, 159–173.

52. Tarque, N.; Benedetti, A.; Camata, G.; Spacone, E. Numerical modelling of the in-plane behaviour of rubble stone masonry. SAHC2014_9th International Conference on Structural Anlysis of Historical Constructions. Mexico City, 2014.

53. Sui, C.; Rafiq, M. Laterally Loaded Masonry Wall Panels: A Review of Numerical Methods. *Masonry International* **2009**, *22*, 47.

54. Lotfi, H.R.; Shing, P.B. Interface model applied to fracture of masonry structures. *Journal of structural engineering* **1994**, *120*, 63–80.

55. Pelà, L.; Cervera, M.; Roca, P. An orthotropic damage model for the analysis of masonry structures. *Construction and Building Materials* **2013**, *41*, 957–967.

56. Tarque, N.; Camata, G.; Spacone, E.; Varum, H.; Blondet, M. Nonlinear dynamic analysis of a full-scale unreinforced adobe model. *Earthquake Spectra* **2014**, *30*, 1643–1661.

57. Midas Fea Manual, 2018.

58. de Witte, F. DIANA finite element user's manual: material library. release 8.1, 2002.

59. Vecchio, F.J.; Collins, M.P. The modified compression-field theory for reinforced concrete elements subjected to shear. *ACI J.* **1986**, *83*, 219–231.

60. Selby, R.G. Three-dimensional constitutive relations for reinforced concrete. *Publ. Dept of Civil Engrg., Univ. of Toronto* **1993**.

61. Gattulli, V.; Lofrano, E.; Paolone, A.; Pirolli, G. Performances of FRP reinforcements on masonry buildings evaluated by fragility curves. *Computers & Structures* **2017**, *190*, 150–161.

62. Rots, J.G. Smeared and discrete representations of localized fracture. In *Current Trends in Concrete Fracture Research*; Springer, 1991; pp. 45–59.

63. Lourenço, P.B. Recent advances in masonry modelling: micromodelling and homogenisation. In *Multiscale modeling in solid mechanics: computational approaches*; World Scientific, 2010; pp. 251–294.

64. Gattulli, V.; Lampis, G.; Marcari, G.; Paolone, A. Simulations of FRP reinforcement in masonry panels and application to a historic facade. *Engineering Structures* **2014**, *75*, 604–618.

65. Manfredi, G.; Lignola, G.P.; Voto, S. Military quarters in Nola, Italy—Caserma Principe Amedeo: Damage assessment and reconstruction of a partially collapsed XVIII century complex. *International Journal of Architectural Heritage* **2013**, *7*, 225–246.

66. da Porto, F.; Guidi, G.; Garbin, E.; Modena, C. In-plane behavior of clay masonry walls: experimental testing and finite-element modeling. *Journal of structural engineering* **2010**, *136*, 1379–1392.

67. Ghiassi, B.; Oliveira, D.V.; Lourenço, P.B.; Marcari, G. Numerical study of the role of mortar joints in the bond behavior of FRP-strengthened masonry. *Composites Part B: Engineering* **2013**, *46*, 21–30.

68. Clementi, F.; Gazzani, V.; Poiani, M.; Antonio Mezzapelle, P.; Lenci, S. Seismic assessment of a monumental building through nonlinear analyses of a 3D solid model. *Journal of Earthquake Engineering* **2018**, *22*, 35–61.
69. Feenstra, P.H. Computational aspects of biaxial stress in plain and reinforced concrete. *PhD thesis, Delft University of Technology* **1993**.
70. Thorenfeldt, E. Mechanical properties of high-strength concrete and applications in design. Symposium Proceedings, Utilization of High-Strength Concrete, Norway, 1987, 1987.
71. Hube, M.A.; Mosalam, K.M. Experimental and Computational Evaluation of Current and Innovative In-Span Hinge Details in Reinforced Concrete Box-Girder Bridges Part 1: Experimental Findings and Pre-Test Analysis. Technical report, 2009.
72. Lourenço, P.B.; Barros, J.; Oliveira, J.T. Shear testing of stack bonded masonry. *Construction and Building Materials* **2004**, *18*, 125–132.
73. CEB-FIP. *CEB-FIP Model Code 1990: Design Code*; Thomas Telford, 1993.
74. Ganz, H.; Thürlimann, B. Versuche über die Festigkeit von zweiachsig beanspruchtem Mauerwerk (Tests on the Biaxial Strength of Masonry). Technical report, Report.
75. Marcari, G.; Manfredi, G.; Prota, A.; Pecce, M. In-plane shear performance of masonry panels strengthened with FRP. *Composites Part B: Engineering* **2007**, *38*, 887–901.
76. Milosevic, J.; Lopes, M.; Bento, R.; Gago, A. Triplet test on rubble stone masonry panels. *CIST, IST, Technical University of Lisbon, Portugal* **2012**.
77. Van der Pluijm, R. Shear behaviour of bed joints **1993**.